Materials & Design 260 (2025) 115097

Contents lists available at ScienceDirect

Materials & Design

journal homepage: www.elsevier.com/locate/matdes

An integrated computational materials engineering framework for process–structure–property mapping in laser powder bed fusion

Fabien Briffod*, Phuangphaga Daram, Masahiro Kusano, Makoto Watanabe

Research Center for Structural Materials, National Institute for Materials Science, 1-2-1 Sengen, Tsukuba, 305-0047 Ibaraki, Japan

HIGHLIGHTS

- Produces comprehensive process–microstructure maps across laser power–speed (P, v).
- Enables systematic microstructure prediction over the full print parameter space.
- Calibrated with single-track experiments; captures conduction–keyhole and texture trends.
- Provides design-ready maps to select process windows for targeted microstructures.

GRAPHICAL ABSTRACT

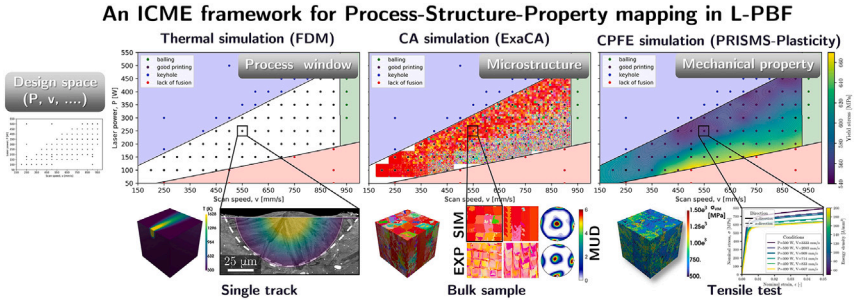

ARTICLE INFO

Keywords:
Additive manufacturing
Crystal plasticity
Microstructure
Cellular automata

ABSTRACT

This work presents a comprehensive, experimentally validated integrated computational materials engineering framework for mapping the process–structure–property relationships in laser powder bed fusion (L-PBF) of Hastelloy-X alloys. The framework couples heat transfer, cellular automata (CA) solidification, and crystal plasticity finite elements (CPFE) simulations within one workflow. The heat transfer model was calibrated using single-track experiments and Bayesian inference to accurately capture melt pool geometry and the transition from conduction to keyhole melting. The CA model, driven by thermal simulation data, successfully reproduced key microstructural features, including the equiaxed-to-columnar grain transition and the formation of a strong crystallographic texture. The mechanical behavior was then predicted by CPFE simulations on representative volume elements extracted from the CA microstructures, revealing a direct correlation between crystallographic texture and macroscopic mechanical properties. The framework was applied to the mapping of the (P,v) process space, identifying distinct regions based on defect formation, microstructure and mechanical response. This validated approach offers a robust and efficient alternative to experimental trial-and-error identification of optimal process window, paving the way for data-driven optimization of L-PBF processes.

1. Introduction

Additive Manufacturing (AM) is transforming the production of metallic structural components by enabling their layer-by-layer fabrication from metal powders or wires, thereby overcoming the limitations of conventional techniques. This technology provides unprecedented design freedom, allowing for the creation of highly complex geometries, refined microstructures, and precisely tailored material properties. These capabilities are crucial for diverse applications across aerospace, medicine, automotive, and industrial design [1–5]. Among various AM

* Corresponding author.
Email address: BRIFFOD.Fabien@nims.go.jp (F. Briffod).

https://doi.org/10.1016/j.matdes.2025.115097
Received 7 September 2025; Received in revised form 4 November 2025; Accepted 6 November 2025
Available online 11 November 2025

methods, laser powder bed fusion (L-PBF) is particularly prominent. While AM processes can be tailored to achieve specific properties for different materials and applications, the vast process parameter space, combined with a limited understanding of the complex underlying multi-scale and multiphysics phenomena, makes optimizing processes through experimental trial-and-error impractical. Consequently, there is a pressing need to develop physics- and data-driven integrated computational materials engineering (ICME) approaches, often termed "digital twins," which couple the various chains within the process–structure–property (PSP) paradigm [6–13].

The prediction of the melt pool dynamics constitutes the core of the process link and can be solved either analytically or with various numerical approaches more or less complex and taking into account different physical phenomena [2,10,14]. Analytical models, often based on analytical solution of the heat equation with a moving heat source, such as the Rosenthal equation, offer fast estimations of melt pool dimensions and temperature fields, providing fundamental insights but typically lacking the fidelity for complex phenomena such as fluid flow and phase change. Besides, the linkages with material properties and process parameters are weak so the domain of application is limited to low energy [15,16]. To capture more detailed thermal behavior, numerical methods like Finite Element Method (FEM) [17,18], Finite Difference Method (FDM) [19,20], and Finite Volume Method (FVM) [13] are employed. These thermal models discretize the domain and solve the heat equation, often incorporating temperature-dependent material properties and latent heat, allowing for more accurate predictions of temperature profiles and solidification fronts. The depth and morphology of the melt pool can also be controlled to a certain extent by varying the heat source model [17,18,21]. However, a comprehensive understanding of melt pool dynamics, including Marangoni convection, recoil pressure, and keyhole formation, necessitates the use of Computational Fluid Dynamics (CFD). CFD models, often coupled with volume-of-fluid (VOF) methods, rigorously solve the Navier-Stokes equations for fluid flow and heat transfer, providing high-fidelity simulations but at a computationally high cost [7,10,22,23].

Microstructure prediction in AM is a complex challenge, often addressed through a combination of analytical and numerical techniques. Analytical approaches provide simplified insights into the relationships between processing parameters and microstructure (e.g., grain size or phase fractions), but they frequently struggle to capture the intricate, non-equilibrium phenomena inherent to rapid solidification [24]. For higher fidelity, phase-field models are utilized. These continuum-based approaches use order parameters that vary smoothly across interfaces, enabling the simulation of complex microstructural evolutions such as dendrite growth, solute segregation, and phase transformations under non-equilibrium conditions [25–29]. However, their high computational cost limits the size of the predicted microstructures and hinders efficient exploration of the process-structure space. To overcome these limitations, mesoscale numerical methods like Cellular Automata (CA) are widely employed [30]. CA simulations discretize the material into a grid of cells, with each cell's state evolving based on predefined rules and neighboring cell states. This approach effectively mimics nucleation, grain growth, and competitive solidification, providing a visual representation of the evolving microstructure [11,19,20,22,31–36]. The CA method is currently the most widely used approach for microstructure prediction, as it offers a reliable and computationally efficient alternative to phase-field models while accurately predicting grain morphology [37,38].

The prediction of mechanical properties in polycrystalline aggregates is typically accomplished through crystal plasticity simulations, using either mean-field homogenization or full-field approaches. Among mean-field approaches, the elastic-viscoplastic self-consistent (EVPSC) method is widely used. This method treats each individual grain as a spherical inclusion embedded within a homogeneous effective medium. It accounts for the grain's crystallographic orientation and its interactions with the surrounding medium using Eshelby's inclusion theory. While computationally fast and effective for predicting macroscopic responses and the evolution of texture, EVPSC fails to capture local heterogeneities at grain boundaries and the influence of grain morphology, as the microstructure is not explicitly modeled. In contrast, full-field approaches, such as the crystal plasticity finite element method (CPFEM) or the crystal plasticity fast Fourier transformation (CPFFT) method, explicitly model each grain within the polycrystal [39–42]. The interactions between neighboring grains are implicitly accounted for and solved directly by the method itself. Although these methods are more computationally demanding than mean-field approaches, they offer significant advantages. They can predict local intragranular heterogeneities that arise from grain interactions and can even incorporate size effects if physics-based, non-local constitutive models are employed. Full-field approaches are thus more widely used for the mechanical predictions of AM materials [8,12,43].

In this study, we developed and experimentally validated an ICME framework that integrates (i) finite-difference thermal predictions, (ii) CA-based grain-scale solidification, and (iii) CPFE-based mechanical response into a single workflow. Beyond validating each link, the central contribution is their integration to generate process-wide maps, systematically linking (P, v) to microstructures and properties.

2. Materials and methods

A general overview of the numerical framework for the PSP linkage is presented in the schematic diagram in Fig. 1. It contains three interconnected modules: (1) thermal field prediction by FDM, (2) microstructure prediction by CA method and (3) mechanical property prediction by CPFEM. The output of one module serves as the input for the subsequent one. Each module is relatively independent and its produced output is validated against a set of specific experiments. A detailed description of each module of the framework together with their corresponding experimental sets is provided hereafter. Throughout the present manuscript, a Cartesian coordinate system (x, y, z) is used where the xy-plane is the build plane and the z-direction is the build direction (BD).

2.1. Thermal field prediction

2.1.1. Constitutive equations

The three-dimensional, transient temperature field, $T(x, y, z, t)$, is determined by solving the governing heat conduction equation:

$$\rho(T)c_p(T)\frac{\partial T}{\partial t} = \nabla \cdot (\lambda(T)\nabla T) + Q \tag{1}$$

where $\rho(T)$, $c_p(T)$, and $\lambda(T)$ are the temperature-dependent material properties: density, specific heat capacity, and thermal conductivity, respectively. The term Q represents the volumetric rate of internal heat generation.

The heat source at a material point located at (x, y, z), distant by $(\Delta x, \Delta y, \Delta z)$ from the center of a moving laser with velocity v and power P is modeled using a three-dimensional, super-Gaussian volumetric heat source distribution [21]:

$$Q_{\text{laser}}(x, y, z) = \frac{\eta P}{V_0}\exp\left(-\left[\left(\frac{\Delta x}{r(z)}\right)^2 + \left(\frac{\Delta y}{r(z)}\right)^2\right]^{k/2}\right) \tag{2}$$

with η the laser absorptivity, V_0 the volume integral of the distribution and k the Gaussian exponent. The variation of the heat source along the depth (z-direction) is controlled by the decay of the radius $r(z)$:

$$r(z) = \frac{2\sigma}{\sqrt[k]{2}}\left\langle 1 - \left|\frac{\Delta z}{d}\right|^m \right\rangle^{1/m} \tag{3}$$

where 2σ is the laser spot radius, d is the heat source depth and m is a volumetric shape parameter. $\langle . \rangle$ represents the Macaulay brackets. Fig. 2 depicts examples of two-dimensional cross-sections of the normalized

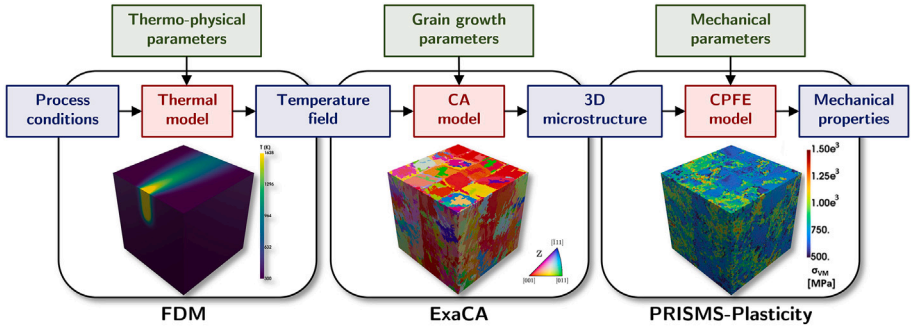

Fig. 1. General overview of the process-structure-property framework.

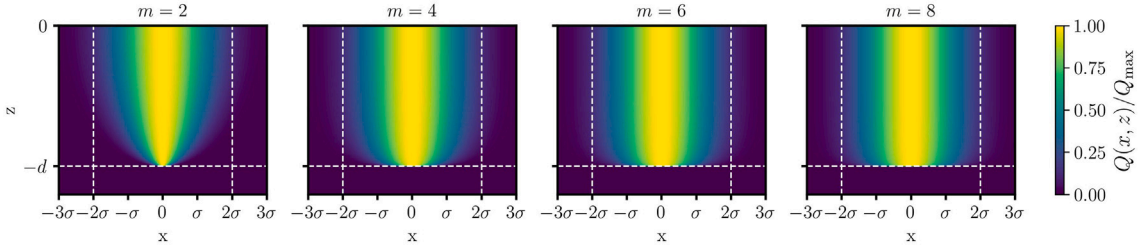

Fig. 2. Examples of cross-sections of the normalized power distribution for k = 2 and m = [2,4,6,8].

power distribution of a Gaussian heat source ($k = 2$) with the volumetric shape parameter m varying between 2 and 8.

Heat loss at a free surface is considered by:

$$Q_{\text{loss}} = h\left(T - T_{\text{amb}}\right) + \sigma_B \epsilon \left(T^4 - T_{\text{amb}}^4\right) \tag{4}$$

where the first and second terms represent the heat loss due to convection and radiation with the atmosphere of temperature T_{amb}, respectively. h is the heat transfer coefficient ($10\ \text{W}\cdot\text{m}^{-2}\cdot\text{K}^{-1}$), σ_B is the Stefan-Boltzmann constant ($5.67 \times 10^{-8}\ \text{W}\cdot\text{m}^{-2}\cdot\text{K}^{-4}$), and ϵ is the emissivity of the free surface taken as 0.3.

The heat equation is solved by the finite difference method (FDM) on a regular mesh of element size d_{elem}, using the forward time-centered space (FTCS) integration scheme. While computationally efficient, the method is conditionally stable due to the explicit time integration scheme and thus requires a maximum time increment Δt given by:

$$\Delta t \leq \frac{d_{elem}^2}{6\kappa} \tag{5}$$

where $\kappa = \lambda/(\rho c_p)$ is the thermal diffusivity of the material.

The present thermal simulation model is based solely on the heat equation (Eq. (1)), thereby omitting critical multiphysics phenomena inherent to the printing process. These include, but are not limited to, laser–material interactions, Marangoni convection within the melt pool, and vaporisation-induced recoil pressure leading to keyholing. Consequently, to accurately capture the transition from conduction-mode to keyhole-mode melting, characterized by a significant increase in melt pool depth and aspect ratio, it is essential to dynamically adjust the heat source depth, d, and the laser absorptivity, η, according to the prevailing process conditions. Recent investigations have established relationships between the normalized melt pool depth, $d^* = d/2\sigma$, a dimensionless parameter β_η (referred to as the Keyhole number or normalized enthalpy, dependent on η), and the normalized thermal diffusion length L_{th}^* [44–46]:

$$d^* = \frac{d}{2\sigma} = 0.6\beta_\eta L_{th}^* = 0.6\left(\frac{\eta P}{\pi h_s \sqrt{\kappa v (2\sigma)^3}}\right)\sqrt{\frac{\kappa}{v(2\sigma)}} \tag{6}$$

where $h_s = \rho c_p (T_m - T_0)$ represents the latent heat of melting, with T_m and T_0 denoting the melting and substrate temperatures, respectively. To enable a more physically predictive capability for the conduction-to-keyhole transition, a two-parameter absorptivity function, dependent on d^*, has been proposed:

$$\eta = \begin{cases} \eta_c & \text{if } \frac{d}{2\sigma} \leq 1 \\ \eta_k \left(1 - e^{-0.66\beta_{\eta_c} L_{th}^*}\right) & \text{if } \frac{d}{2\sigma} > 1 \end{cases} \tag{7}$$

Here, η_c and η_k are the laser absorptivity values for the conduction and keyhole modes, respectively; η_c is typically assumed constant. During keyholing, the laser absorptivity progressively increases towards η_k. By estimating these two absorptivity parameters, this approach allows for the physical prediction of melt pool depth across a range of process conditions.

2.1.2. Single-track experiments

To calibrate the thermal model parameters, specifically the laser absorptivities (η_c and η_k) and heat source shape parameters (k and m), a series of single-track experiments were conducted on a Hastelloy-X substrate in a previous study [47]. These experiments were performed at room temperature using an SLM 280 HL system (SLM Solutions, Germany), equipped with a Gaussian laser operating at a spot radius of $2\sigma = 40$ µm. No powder was used during these calibration tests. Laser power was varied from 50 to 700 W, while the scanning speed ranged from 250 to 3500 $\text{mm}\cdot\text{s}^{-1}$. This combination of parameters resulted in linear energy densities, $E = P/(4\sigma v)$, spanning from 0.7 to 35 $\text{J}\cdot\text{mm}^{-2}$. Following the laser processing, the cross-sections of each track were prepared by metallographic polishing and etching, then examined using scanning electron microscopy (SEM). Melt pool depth, width, and width at half-depth were extracted from the SEM images. These measurements were subsequently used to calibrate the laser absorptivities, while the heat source shape parameters were fitted to accurately reproduce the observed melt pool morphology.

2.1.3. Single-track simulations

Single-track simulations were performed using the established heat transfer model and calibrated absorptivity parameters. For these

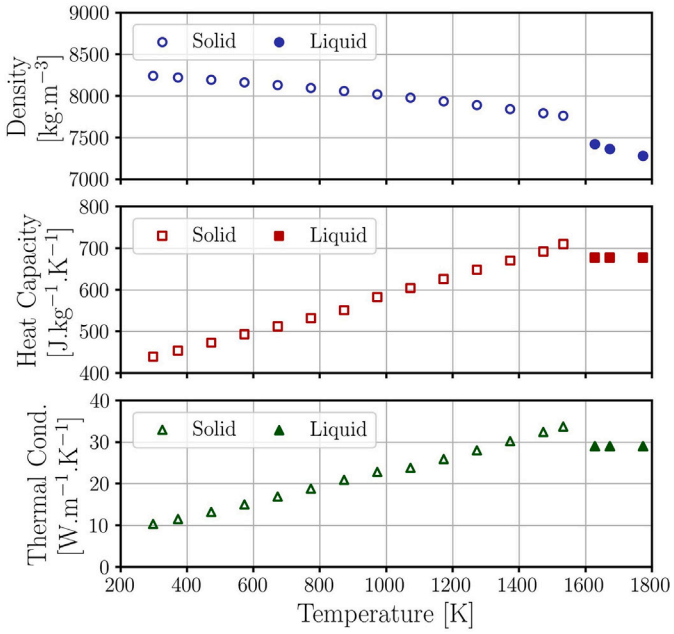

Fig. 3. Thermophysical properties of Hastelloy-X taken from literature [48].

simulations, the heat source depth in Eq. (3) was assumed to correspond to the melt pool depth, consistent with Eq. (6). A cubic domain measuring 1.5 × 1.5 × 1.5 mm was discretized with a uniform grid of 10 μm elements. The laser, simulating a Gaussian beam as used in experiments (hence, the Gaussian exponent k was set to 2), traveled along the x-direction from one edge of the domain to the opposite, centered along the y-axis. To evaluate the impact of the volumetric shape parameter, four distinct m values were tested: 2, 4, 6, and 8. The same laser power and velocity conditions from the experimental calibration were applied. Subsequently, simulated melt pool depths were extracted and compared against experimental data, and cross-sections were also generated for comparison with SEM micrographs. The thermo-physical properties (ρ, c_p, λ) of the H-X alloy were taken from literature [48] and are reported in Fig. 3.

2.2. Microstructure prediction

2.2.1. Cellular automata method

The prediction of the solidified microstructure at the polycrystalline scale due to the AM process is carried out using the cellular automata method (CA), with the open-source software ExaCA [35].

In the CA framework, the computational domain is discretized into a grid of cells, each existing in a liquid, solid, or active state. The active state represents the solidification front. The model phenomenologically approximates the complex dendritic structure of a growing grain with a regular octahedron, whose vertices align with the preferential ⟨100⟩ crystallographic growth directions. A liquid cell transforms to solid once its center is enveloped by a neighboring growing grain. To minimize grid-induced growth anisotropy, the model employs the decentered octahedron algorithm, which prevents growth from being biased along the grid axes [30].

The growth velocity, v, of the octahedral envelope's vertices is governed by the local undercooling ΔT. This relationship is defined by an interfacial response function, which is expressed as a third-order polynomial derived from the Kurz-Giovanola-Trivedi (KGT) model [24]:

$$v(\Delta T) = A\Delta T^3 + B\Delta T^2 + C\Delta T + D \tag{8}$$

where A, B, C and D are material-dependent fitting parameters.

Heterogeneous nucleation is implemented using a stochastic model. Based on an initial nucleation density, N_0, a fraction of cells are designated as potential nucleation sites. Each potential site is assigned a critical nucleation undercooling value:

$$\Delta T = \Delta T_0 + \mathcal{N}(\Delta T_N, \Delta T_\sigma) \tag{9}$$

sampled from a Gaussian distribution, $\mathcal{N}$, with a mean ΔT_N and standard deviation ΔT_σ. A new grain forms if a site reaches its assigned undercooling before being captured by an adjacent growing grain. The newly formed grain is then assigned a random crystallographic orientation.

2.2.2. Characterization of as-built microstructure

The microstructures of as-built Hastelloy-X specimens were analyzed from previous studies [49,50]. Cylindrical samples, measuring 10 mm in diameter and 8 mm in height, were fabricated using the same SLM machine as employed for the single-track experiments. These specimens were built on a SUS304 substrate with a 3 mm supports. A gas-atomized Hastelloy-X powder (Amperprint®0228.074, Höganäs) with an average particle diameter of 30 μm was used. The processing parameters included an individual layer thickness of 30 μm and a zig-zag scan strategy with a ±90° rotation between successive layers. The hatching distance was set to 100 μm. Six distinct samples were fabricated under varying laser power (ranging from 300 to 500 W) and scan speed (from 667 to 3333 mm·s^{-1}) so that the energy density $E = P/(vhl)$ (h is the hatching distance and l the layer thickness) ranges between 50 and 200 J·mm^{-3}. Microstructural investigations were conducted using electron backscattered diffraction (EBSD) on both the xy- and xz-planes, following standard metallographic polishing procedures.

2.2.3. Cellular automata simulation procedure

CA simulations were performed to predict microstructures under the same processing conditions as those used in our experiments. These simulations were conducted on a square domain measuring 600 × 600 μm (xy-plane), with an element size of 2.5 μm. The initial domain size of the substrate in the z-direction was automatically adjusted to match the melt pool depth for each specific processing condition. Fig. 4 illustrates the simulation procedure for two successive layers. At the beginning of each layer, a powder layer, composed of randomly sampled crystal orientations, was added to the top surface of the previously built microstructure. Consistent with the experimental layer thickness of 30 μm, the powder layer was represented by 12 cells in the z-direction. Thermal fields from the single-track simulations served as input for the CA model. Specifically, we extracted the coordinates, melting and solidification times, and cooling rates for elements that exceeded the material's melting temperature. These thermal data were then repeated, translated, and rotated to accurately replicate the experimental scanning strategy. In the framework, the scanning direction was set along the x-axis for odd layers and the y-axis for even layers. Each simulation was run for a total of 50 layers. The parameters used in the CA simulations are summarized in Table 1. The time step, Δt, was dynamically adjusted for each simulation based on the ratio between the cell size, d_{elem} and the scan speed v:

$$\Delta t = \xi \frac{d_{elem}}{v}. \tag{10}$$

A value of $\xi = 0.04$ was selected based on previous studies [35,36,51] to ensure time-independent results.

2.3. Mechanical property prediction

2.3.1. Crystal plasticity finite element method

The macroscopic mechanical response of polycrystals is predicted using the CPFEM, implemented within the open-source software PRISMS-Plasticity [41]. This framework employs a finite strain formalism, where the total deformation gradient tensor **F** is multiplicatively decomposed

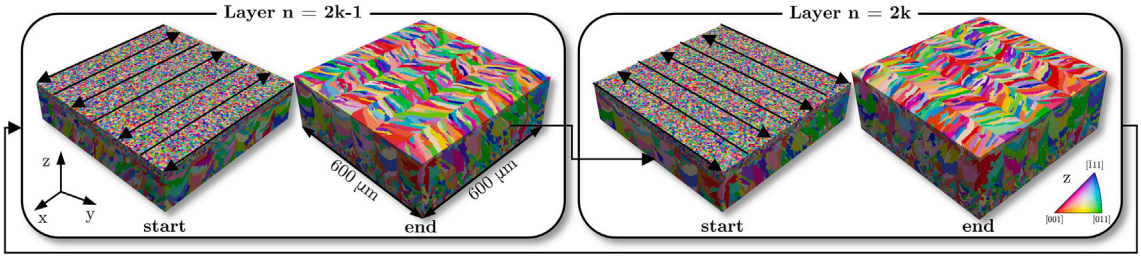

Fig. 4. Schematic diagram of the the simulation of two successive layers by cellular automata.

Table 1
AM CA simulation parameters.

Parameter	Value
Cell size, d_{elem} [μm]	2.5
Time step, Δt, [μs]	0.03–0.15
Interfacial response, A [m·s^{-1}·K^{-3}]	3.15×10^{-6}
Interfacial response, B, [m·s^{-1}·K^{-2}]	4.6×10^{-10}
Interfacial response, C [m·s^{-1}·K^{-1}]	0.0
Interfacial response, D [m·s^{-1}]	0.0
Heterogeneous nucleation density, N_0 [m^{-3}]	1×10^{12}
Mean nucleation undercooling, ΔT_N, [K]	5
Std. dev. of nucleation undercooling, ΔT_σ [K]	0.5
Hatching distance [μm]	100
Layer thickness [μm]	30
Number of layers simulated [-]	50

Table 2
Crystal plasticity parameters taken from literature [49,53].

Parameter	Value
C_{11} [GPa]	230.4
C_{12} [GPa]	156.12
C_{44} [GPa]	121.77
τ_0^β [MPa]	247
τ_s^β [MPa]	700
h_0^β [MPa]	240
a^β [-]	0.01

into elastic ($\mathbf{F}_e$) and plastic ($\mathbf{F}_p$) components [52]:

$$\mathbf{F} = \mathbf{F}_e \mathbf{F}_p. \tag{11}$$

Here, $\mathbf{F}_e$ accounts for the rigid-body rotation and elastic stretching of the crystal lattice, while $\mathbf{F}_p$ captures the inelastic deformation. Plasticity in this model is solely attributed to dislocation slip on N_s distinct slip systems. The plastic velocity gradient, $\mathbf{L}_p$, is consequently defined as:

$$\mathbf{L}_p = \dot{\mathbf{F}}_p \mathbf{F}_p^{-1} = \sum_{\alpha=1}^{N_s} \dot{\gamma}_s^\alpha \mathbf{m}_s^\alpha \otimes \mathbf{n}_s^\alpha \mathrm{sign}(\tau^\alpha), \tag{12}$$

where $\dot{\gamma}_s^\alpha$, $\mathbf{m}_s^\alpha$ and $\mathbf{n}_s^\alpha$ are the shear strain rate, slip direction vector and slip normal vector of the slip system α, respectively. The resolved shear stress τ^α on each slip system is calculated from the second Piola-Kirchhoff stress tensor $\mathbf{S}$:

$$\tau^\alpha = \mathbf{S} : \mathbf{m}_s^\alpha \otimes \mathbf{n}_s^\alpha. \tag{13}$$

Plastic flow on individual slip systems is governed by a rate-independent yield criterion based on Schmid's law:

$$f^\alpha = |\tau^\alpha| - \tau_c^\alpha \tag{14}$$

where τ_c^α represents the critical resolved shear stress (CRSS) or slip resistance of slip system α. The evolution of τ_c^α is coupled to the accumulated plastic activity across all slip systems through a phenomenological hardening law:

$$\dot{\tau}_c^\alpha = \sum_{\beta=1}^{N_s} h^{\alpha\beta} \dot{\gamma}^\beta. \tag{15}$$

The hardening modulus $h^{\alpha\beta}$, which quantifies the influence of slip on system β on the hardening of system α, follows a power-law relationship:

$$h^{\alpha\beta} = h_0^\beta q^{\alpha\beta} \left[1 - \frac{\tau_0^\beta}{\tau_s^\beta} \right]^{a^\beta}, \tag{16}$$

with h_0^β representing the initial hardening rate, τ_0^β the initial slip resistance, τ_s^β the saturated slip resistance, and a^β the power-law exponent for slip system β. The latent hardening ratio, $q^{\alpha\beta}$, is set to 1.0 for coplanar slip systems and 1.4 for non-coplanar systems, reflecting the stronger interaction between dislocations on intersecting slip planes.

2.3.2. Tensile testing of as-built specimens

Tensile responses in both the x- and z-directions were obtained from previous studies [49,50]. Dog-bone tensile samples were directly fabricated within the SLM machine, with their tensile axes aligned specifically along either the x- or z-direction. The build conditions for these tensile samples mirrored those used for microstructural characterization. Following fabrication, the samples underwent annealing at 823 K for one hour to relieve residual stresses. They were then cut from the substrate using electric discharge machining. The surface of the tensile test specimens was polished manually, in sequence, from coarse grinding to the diamond slurry of 9, 3, and 1 μm. Tensile tests were conducted at room temperature, at a constant cross-head speed until failure. Strain was precisely measured using a strain gauge (KFEL-2–120-C1L3M2R, KFEM-1–120-C1L3M2R, Kyowa Electric Industry Co., Ltd., Japan) up to approximately 10 % strain.

2.3.3. Crystal plasticity simulations

Cubic representative volume elements (RVEs), each measuring $400 \times 400 \times 400$ μm, were extracted from the microstructures generated by the CA simulations. These RVEs were meshed using $80 \times 80 \times 80$ regular hexahedral elements with linear integration (C3D8). Uniaxial tensile strain was then applied to these RVEs, either in the x- or z-direction, mirroring the experimental tensile test conditions. The cubic elasticity and crystal plasticity parameters for the Hastelloy-X material were adopted from previous studies [49,53] and are summarized in Table 2. Consistent with the face-centered cubic (fcc) crystal structure of Hastelloy-X, all twelve $\{111\}\langle 1\bar{1}0\rangle$ slip systems were considered in the simulations.

3. Results and discussion

3.1. Melt pool analysis

3.1.1. Melt pool analysis from single-track experiments

Fig. 5(a–d) presents cross-sectional SEM micrographs, taken perpendicular to the scanning direction, from single-track experiments. These images showcase the evolution of melt pool morphology at a constant scanning speed of $v = 500$ mm·s^{-1} across varying laser powers: (a)

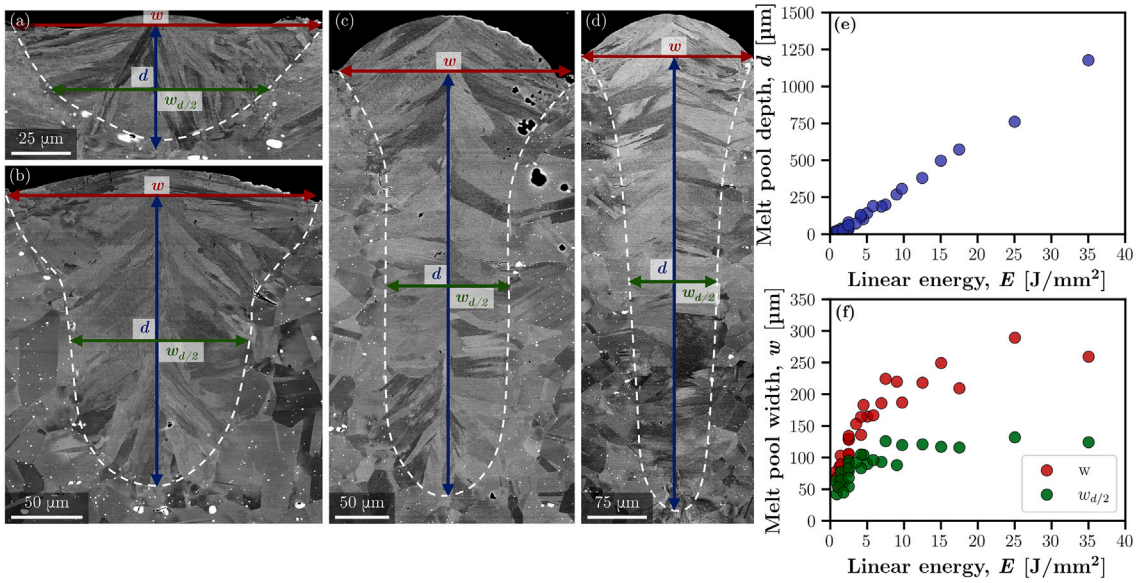

Fig. 5. (a–d) Examples of cross-sectional SEM micrographs for the single-track experiments at (a) P = 100 W, (b) P = 300 W, (c) P = 500 W and (d) P = 700 W with v = 500 mm.s^{-1}. (e) Distribution of melt pool depth d and (f) melt pool width w and width at half-depth $w_{d/2}$ against the linear energy E.

P = 100 W, (b) P = 300 W, (c) P = 500 W, and (d) P = 700 W. Each micrograph highlights the defined melt pool boundaries, along with the measured depth and width. The distinct grain morphology inside and outside the melt pool, coupled with the rapid solidification preventing inclusion formation within the melt pool (visible as bright regions outside), facilitates the clear identification of these boundaries. Melt pool depth was measured from the flat surface, intentionally excluding any raised convex regions. At lower energy densities, as seen in Fig. 5(a), the melt pool exhibits a semi-circular shape, which is characteristic of the conduction-mode regime. As the energy density increases, the melt pool depth progressively rises. Furthermore, the melt pool shape begins to display an inflection region, below which its width tends to remain constant. The comprehensive distribution of melt pool depth and width across all single-track conditions is summarized in Fig. 5(e and f). A strong linear relationship ($R^2 = 0.99$) is observed between the melt pool depth and the linear energy density. Conversely, while the melt pool width also increases with energy density, it shows a clear saturation trend. This saturation is particularly evident for the width at half-depth, which plateaus at approximately 140 µm above a linear energy density of 5 J·mm^{-2}. A similar analysis was also carried out for single-track experiments including a single layer of powder. The resulting melt-pool geometries showed only minor differences from those obtained without powder, confirming that the powder layer exerts a limited influence on the calibration procedure. The corresponding experimental data are provided in the Supplementary Materials.

3.1.2. Calibration of laser absorptivity parameters

To calibrate the laser absorptivity parameters (η_c, η_k) in Eq. (5), the estimated melt pool depths from the single-track experiments were used, along with the thermophysical properties of the material at melting temperature (Fig. 3) and laser process conditions. The calibration was performed using a Bayesian inference framework with a Markov Chain Monte Carlo (MCMC) method, specifically the Metropolis-Hastings algorithm, to robustly sample the posterior distributions of the model parameters. The algorithm functioned by defining a log-likelihood function that quantified the agreement between the model's predicted melt pool depths and the experimental observations. We assumed a Gaussian error model with an estimated standard deviation (σ). At each step of the MCMC simulation, new parameter sets for (η_c, η_k, σ) were proposed from a multivariate normal distribution centered on the current parameter values. The acceptance or rejection of these proposed sets was determined by comparing their likelihood to that of the current parameters. After an initial burn-in phase to ensure chain convergence, and subsequent thinning, the collected samples effectively mapped the posterior probability distributions for each parameter. The mean values of these posterior distributions were then taken as the most probable estimates, yielding $\eta_c = 0.2926$ and $\eta_k = 0.6206$. For comparison, parameter optimization through minimization of the mean squared error between predicted and experimental depths resulted in $\eta_c = 0.2757$ and $\eta_k = 0.6210$. These values are notably close to the MCMC results and align well with estimates from previous studies [44,46]. Fig. 6(a) presents the estimated absorptivity as a function of $\beta_\eta L^*_{th}$, while Fig. 6(b) shows the experimental normalized depth as a function of $\beta_\eta L^*_{th}$. With the calibrated absorptivity parameters, Eq. (6) demonstrates excellent agreement with the experimental data, achieving an $R^2 = 0.9949$. To evaluate the sensitivity of the calibration to the number of experimental data points, additional fitting procedures were carried out by progressively reducing the number of single-track conditions used for parameter estimation. The results, provided in the Supplementary Materials, show that the keyhole-mode absorptivity (η_k) remains nearly constant regardless of the number of fitting points, while the conduction-mode absorptivity (η_c) converges reliably when approximately ten well-distributed conditions are considered.

3.1.3. Melt pool prediction from single-track simulations

Fig. 7(a) illustrates the predicted versus experimental melt pool depths for all four m values. Interestingly, the m value showed limited influence on the predicted melt pool depth, with most simulations accurately capturing the experimental depths for most of the conditions. This supports the initial assumption that the heat source depth can reasonably approximate the melt pool depth. Fig. 7(b) overlays the predicted melt pool cross-sections for the four m values onto the experimental SEM micrographs (as shown in Fig. 2a–d). In the conduction mode (P = 100 W), all four simulations predict a similar semi-circular melt pool. While the simulated top surface widths are slightly smaller than experimental values, the widths at half-depth show reasonable agreement. This indicates that in the conduction regime, the volumetric shape parameter has a limited effect on melt pool morphology. However, at higher laser powers, keyholing occurs, leading to a significant increase in melt pool depth. For m = 2, the model tends to slightly underestimate the melt pool depth and,

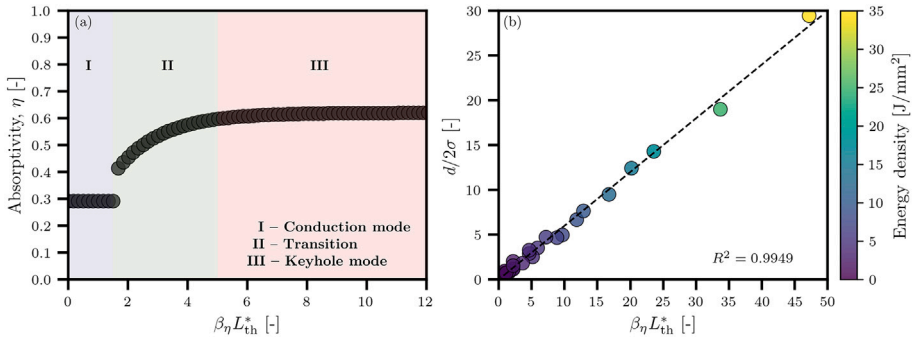

Fig. 6. (a) Estimated absorptivity as a function of $\beta_\eta L^*_{th}$. (b) Predicted normalized melt pool depth as a function of $\beta_\eta L^*_{th}$.

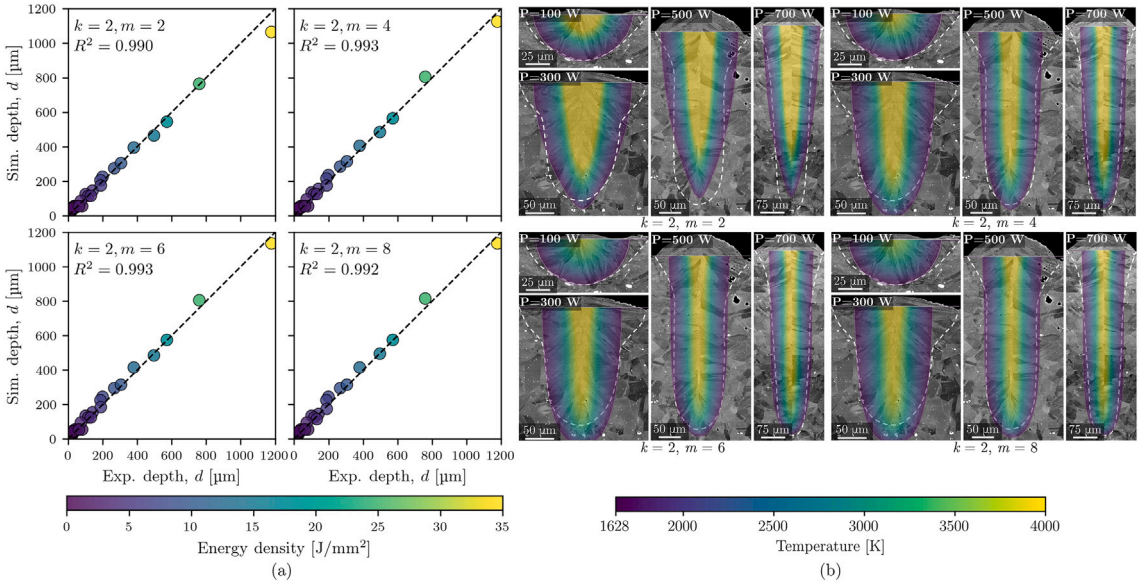

Fig. 7. (a) Comparison between simulated and experimentally measured melt pool depths across all investigated experimental conditions, shown for four values of the material parameter m (2, 4, 6, and 8). (b) Cross-sectional SEM micrographs of the melt pools, overlaid with the corresponding simulated melt pool profiles calculated for the four m values.

notably, incorrectly predicts a sharp, pointy tip for the melt pool bottom, particularly visible at P = 500 W and P = 700 W. Increasing the m parameter effectively flattens the bottom of the melt pool, showing much better agreement with experimental observations. Conversely, increasing m also tends to slightly overestimate the melt pool depth, especially for m = 8. Considering these trade-offs, a value of m = 6 appears to yield the most reasonable agreement with experimental melt pool morphology and depth predictions.

3.2. Microstructure analysis

3.2.1. Experimental microstructures

The EBSD map with IPF color coding along the build direction is presented in Fig. 8(a and b) for the as-built microstructures on both the xy- and xz-planes, sorted by increasing energy density. The xy-plane maps clearly reveal the regular grid pattern characteristic of the applied scan strategy, while the xz-plane maps distinctly show the melt pool morphology. As energy density increases, a trend towards larger grain sizes is observed. This transition progresses from fine grains exhibiting a V–shaped morphology at low energy densities (50–80 J·mm^{-3}) to dominant columnar grains that grow epitaxially along the build direction at high energy densities. The (100) pole figures derived from the xy-plane EBSD data are also provided in Fig. 8(c). These figures demonstrate a progressive transition from a nearly random texture to a strong cube texture, where the ⟨100⟩ directions increasingly align with the x-, y-, and z-axes. This textural evolution is commonly observed with a zig-zag scanning pattern combined with a ± 90° rotation between successive layers [54,55]. Furthermore, it is noteworthy that at higher energy densities, individual grains exhibit local variations in crystal orientation, suggesting the presence of residual stress or accumulated strain within the as-built material [56].

3.2.2. Numerical microstructures

CA simulations were performed using the same laser conditions as in the experiments, across the four volumetric shape parameters (m). Fig. 9(a) displays the predicted microstructures after 50 layers for m = 6, with results for other m values provided in the Supplementary Materials. Animations of the solidification process for ten consecutive layers at two representative process conditions (P = 500 W, v = 2083 mm·s^{-1} and P = 400 W, v = 833 mm·s^{-1}) are provided in the Supplementary Materials to illustrate the evolution of melt-pool geometry and microstructure under different energy densities. For each microstructure, the layers affected by the laser scan of the final layer were removed. Two-dimensional EBSD maps, with IPF color coding along the z-direction, are presented for the xy- and xz-planes in Fig. 8(b and c). The CA model accurately reproduces the observed equiaxed-to-columnar grain transition with increasing energy density. This is

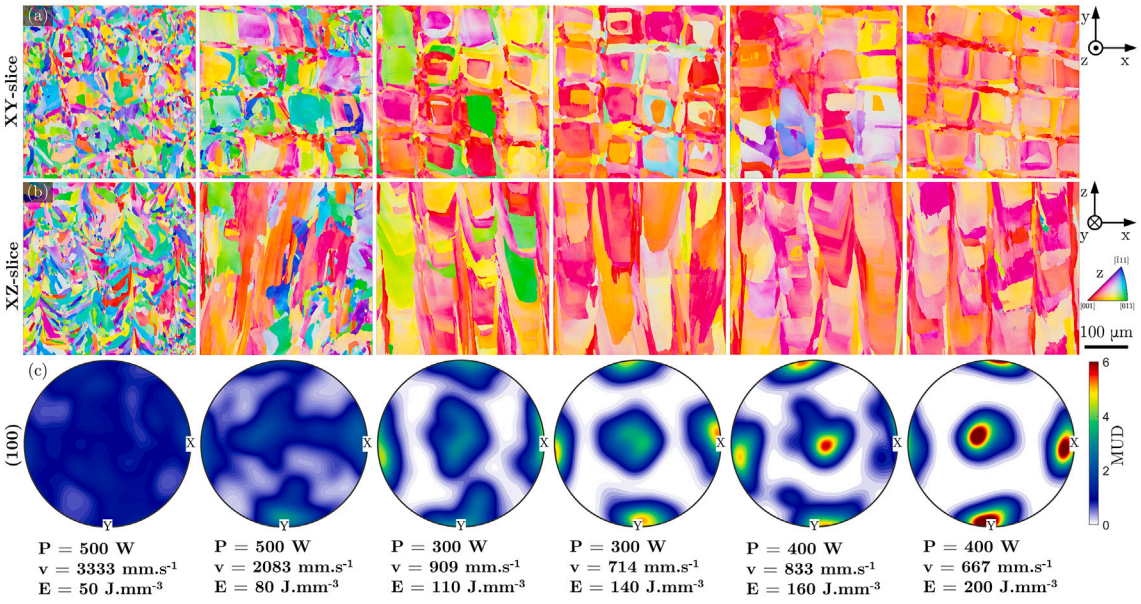

Fig. 8. EBSD maps with IPF color coding along the z-direction on (a) the xy-planes and (b) the xz-planes for the different built samples. (c) Corresponding (100) pole figures calculated from the xy-plane EBSD maps.

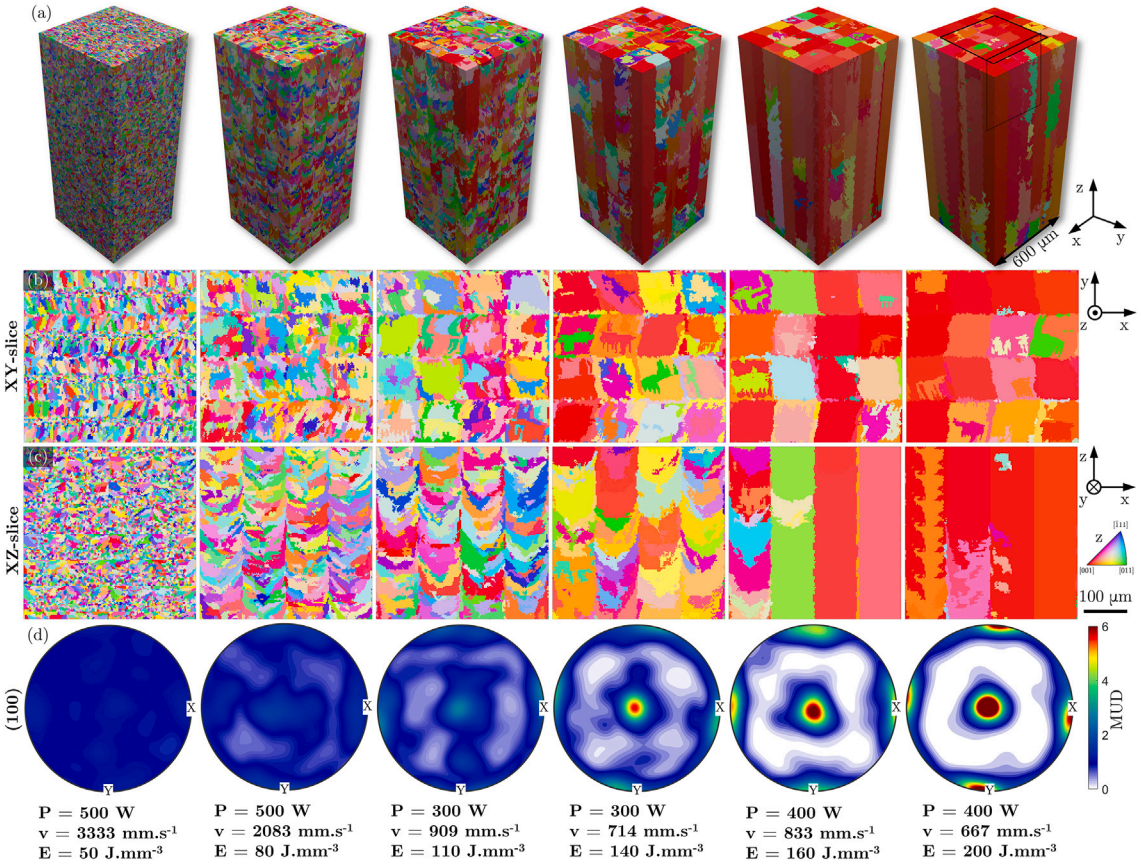

Fig. 9. (a) Numerical microstructure predicted by CA simulations for k = 2 and m = 6 after 50 layers. Cross-section EBSD maps with IPF color coding along the z-direction on (b) the xy-plane and (c) the xz-plane. (d) (100) pole figures calculated from the top xy-plane of the microstructure in (a).

evidenced by the characteristic chessboard pattern visible in the xy-slices and the progressive appearance of columnar grains growing along the z-direction in the xz-slices. Furthermore, the model effectively captures the evolution of crystallographic texture with energy density, as demonstrated by the (100) pole figures in Fig. 9(d), which show a gradual emergence of a $\{001\}_z\langle100\rangle_x$ texture. At low energy densities (below 110 J·mm^{-3}), microstructures predicted with different m values are very similar. This consistency aligns with the finding that melt

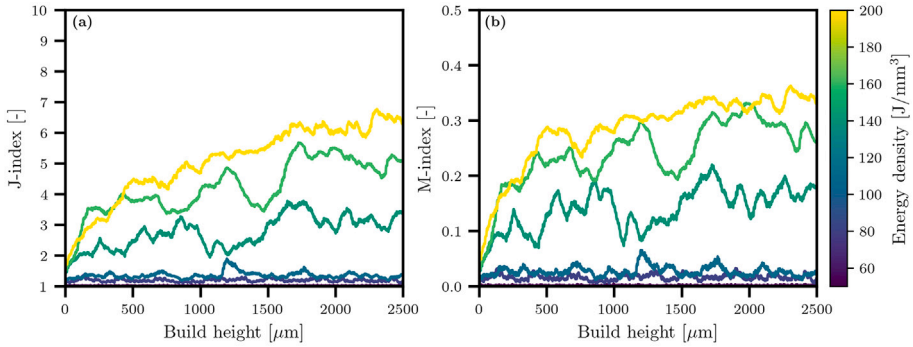

Fig. 10. Evolution of (a) the J-index and (b) the M-index along the build height.

pool shape is relatively independent of the m value in the conduction regime (Fig. 7b). However, as energy density increases, differences due to varying m values become more pronounced, particularly at the highest energy density of 200 J·mm^{-3}. Here, the simulation with m = 2 predicts a decrease in the $\{001\}_z\langle100\rangle_x$ texture strength. This is likely attributable to the sharp, pointy melt pool shape in the keyhole regime (Fig. 7b), which hinders the selection and epitaxial growth of $\{001\}_z$ orientations. Conversely, predictions for m = 4 show an overly rapid strengthening of the $\{001\}_z\langle100\rangle_x$ texture with linear energy density, while the opposite trend is observed for m = 8. Additionally, for m = 2 and m = 4, the simulations rarely predict the formation of small grains separating the chessboard patterns, which were observed experimentally (Fig. 8a and b). These findings collectively underscore that melt pool morphology, in terms of both shape and width, is a critical factor controlling texture formation in AM samples.

To confirm the achievement of a steady-state microstructure, the CA simulations were extended to 100 layers. The evolution of two key texture quantification metrics, the J-index and the M-index, was investigated along the build height. The J-index is defined as:

$$J = \int f(g)^2 dg \tag{17}$$

where $f(g)$ represents the orientation distribution function (ODF) for an orientation g, and dg is a volume element of the orientation space. The J-index ranges from a value of 1 for a completely random microstructure (uniform ODF) to infinity for a single-crystal microstructure. The M-index is defined as [57]:

$$M = \frac{1}{2}\int |f^{\mathrm{U}}_{\mathrm{MDF}}(\theta) - f_{\mathrm{MDF}}(\theta)| d\theta \tag{18}$$

where $f^{\mathrm{U}}_{\mathrm{MDF}}$ denotes the uncorrelated misorientation distribution function (MDF) of a random uniform distribution, and f_{MDF} is the experimentally obtained MDF from EBSD data. The M-index ranges from 0 for random microstructure to 1 for single crystal. Both the J-index and M-index were calculated for each xy-slice along the build direction and are presented in Fig. 10 for the same conditions as in Fig. 9. At low energy densities (below 110 J·mm^{-3}), both indices remain low, indicating that the texture stays close to random (Fig. 9d). Consequently, the build height shows limited influence on texture evolution in this regime. At higher energy densities, both indices demonstrate a rapid increase within the first few hundreds of micrometers, progressively stabilizing thereafter. The observed oscillations in both indices are attributed to the relatively small domain size (600 × 600 μm), which contains 36 square domains defined by the scan pattern and hatching distance. This means any change in crystal orientation within one of these squares can affect both indices substantially. Consistent with other studies [36], these results suggest that a steady-state microstructure is achieved after approximately 1 mm of build height, confirming that 50 layers were sufficient for the present study.

To quantitatively compare the microstructures predicted by the CA model with the experimental EBSD maps, the mean equivalent grain size and M-index were computed from the xy-slices and are reported in Fig. 11. With increasing energy density, both grain size and M-index increase, reflecting enhanced epitaxial grain growth and stronger texture development. The same trend is captured by the CA simulations. Beyond approximately 160 J·mm^{-3}, the average grain size tends to saturate around 80 μm in the experiments and 100 μm in the simulations. This difference arises because, in the simulations, each square region defined by the laser scan pattern is typically filled by a single grain, whereas in the experiments, smaller elongated grains are occasionally observed along the laser path, slightly reducing the average size. The standard deviation of the grain size distribution, shown as error bars in Fig. 11(a), increases with energy density due to the smaller number of grains within the analyzed domain, leading to higher statistical uncertainty. Overall, the predicted grain size evolution exhibits good agreement with the experimental measurements. Regarding texture, the increase in M-index

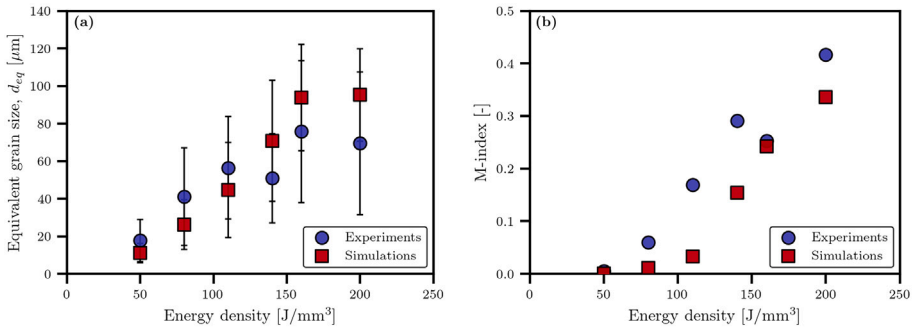

Fig. 11. Comparison of (a) equivalent grain size and (b) M-index obtained from xy-slices of experimental and simulated microstructures.

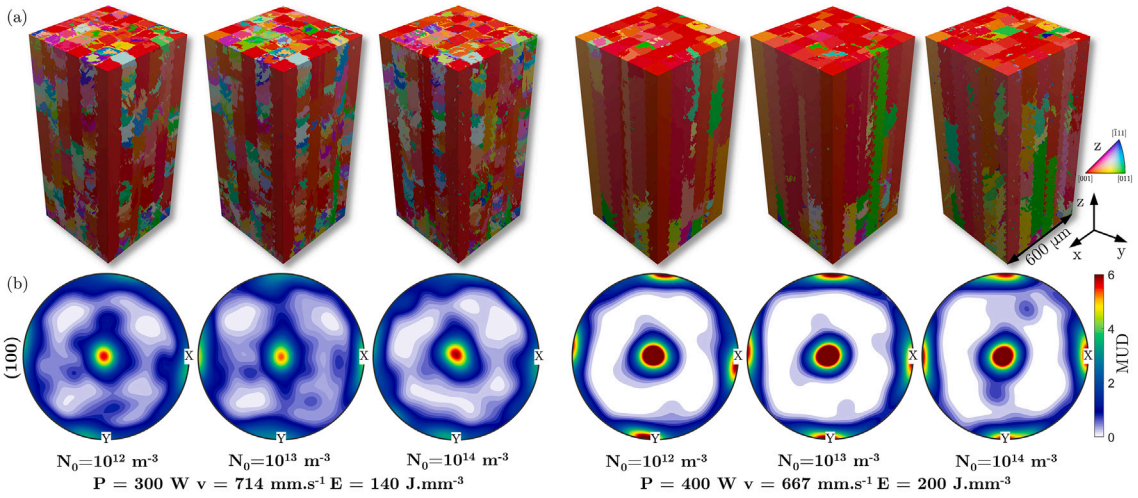

Fig. 12. (a) Microstructure and (b) corresponding (100) pole figure for two different process conditions and three different nucleation densities.

with energy density follows the same trend as in the experiments, albeit slightly shifted by 20–30 J·mm^{-3}. This offset may result from the simplified thermal history used in the CA simulations, which were based on single-track data and therefore neglect the cumulative temperature rise during multi-layer building that reduces the local cooling rate.

The effect of the nucleation density N_0 was finally investigated by simulations identical to those in Fig. 9, comparing the original $N_0 = 1 \times 10^{12}$ m^{-3} with two higher densities: $N_0 = 1 \times 10^{13}$ m^{-3} and $N_0 = 1 \times 10^{14}$ m^{-3}. The results for two selected printing conditions are reported in Fig. 12. Increasing the nucleation density has two effects: (i) promoting small, randomly oriented grains (Fig. 12a) thus decreasing the texture strength of the steady-state microstructure (Fig. 12b) and (ii) modifying the number of layers necessary to reach the steady-state microstructure. However, the present results show that within the range of $N_0 = 1 \times 10^{12}$ to $N_0 = 1 \times 10^{14}$ m^{-3} the predicted steady-state microstructures are relatively similar. This indicates that epitaxial growth predominantly controls the steady-state microstructure in this parameter range.

3.3. Mechanical property analysis

The stress–strain curves of the tensile tests for four different conditions and two loading directions are reported in Fig. 13(a) up to 5 % strain. At $P = 500$ W and $v = 3333$ mm·s^{-1}, the sample deformed along the build direction broke near yielding due to the high density of defects in the sample [50]. For other conditions, the total elongation was above 10 % but since the CP model does not include any damage mechanism, the present study focuses on the early deformation stage. Overall, the yield stress of the material decreases with the energy density. The experiments also tend to highlight a certain anisotropy between specimens loaded in the x- and z-direction.

RVEs of size 400 × 400 × 400 µm were extracted for subsequent CPFE simulations from the top of the simulated microstructures in Fig. 9(a), as shown in Fig. 14(a). The stress–strain curves predicted by CPFE are shown in Fig. 13(b) for all the experimental conditions. Overall, the simulations correctly predicted the yield stress decrease with the energy density as well as a progressive decrease in the Young's modulus. Since the same CP parameters were used for all the simulations and as the model does not include any size effect (Hall-Petch), this suggests that the decrease in yield stress is mostly associated with the $\{001\}_z\langle 100\rangle_x$ texture increase as this orientation leads to nearly maximum Schmid factor for most grains as well as the lowest elastic stiffness. Overall, limited to no anisotropy is predicted between the two loading directions, suggesting that additional mechanisms, not accounted for in the present CP model, may be responsible for this observation. The yield strength anisotropy can be associated with the difference in effective grain size for tensile loading parallel or perpendicular to the build direction, as the elongated columnar grains produce distinct mean free paths for dislocation motion in the two orientations [58,59]. With increasing energy density, the discrepancy between the grain size in the XY and XZ planes widens (Fig. 8), and so does the experimental plastic anisotropy (Fig. 13a), consistent with a Hall–Petch type strengthening behavior. The current CPFE model, however, is formulated in a local

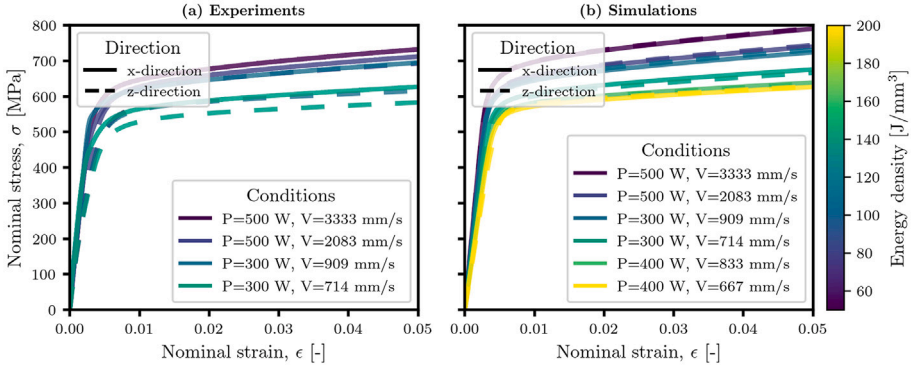

Fig. 13. (a) Experimental and (b) numerical stress-strain curves.

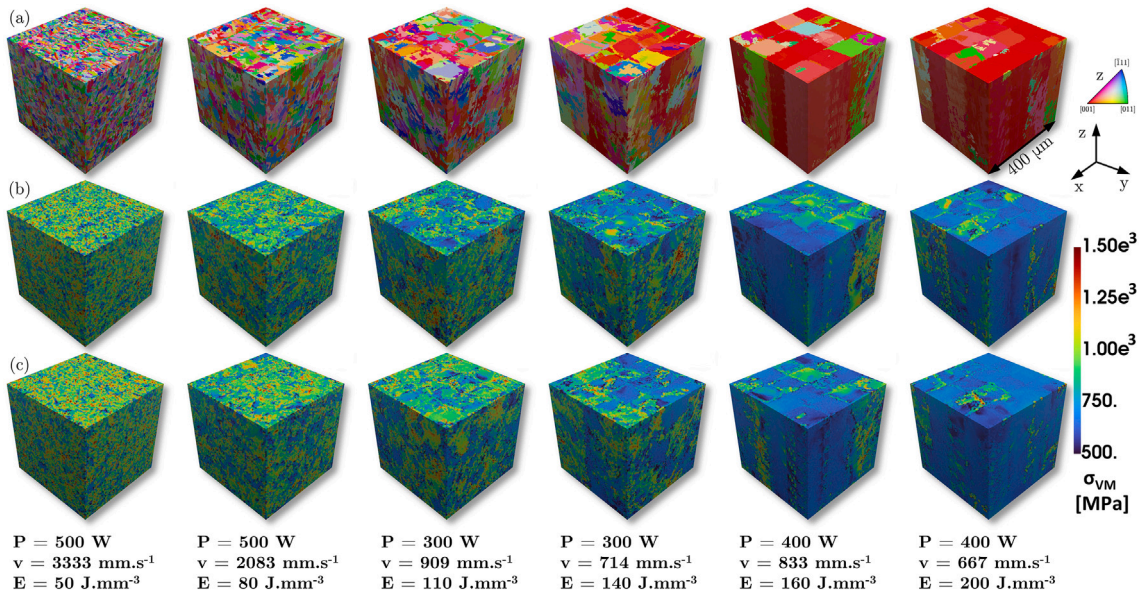

Fig. 14. (a) RVE extracted from the top of the microstructure in Fig. 9(a) colored with IPF color coding along the z-direction. Corresponding von Mises stress at 5 % for uniaxial tensile strain along (b) the x-direction and (c) the z-direction.

framework without explicit size-dependent hardening or geometrically necessary dislocation (GND) evolution, and thus tends to underestimate the anisotropy in the elasto-plastic regime [59].

The von Mises stress fields at 5 % strain are reported in Fig. 14(b and c) for all RVEs and both loading directions. The results indicate that an increase in the $\{001\}_z\langle100\rangle_x$ texture leads to a decrease in the average Mises stress but also results in a more uniform distribution within the microstructure. Furthermore, grains exhibiting orientations close to the ideal Cube orientation tend to show similar stress distributions irrespective of the loading direction. Conversely, significant stress accumulation is observed primarily near interfaces between grains with high misorientation angles.

3.4. Process-structure-property mapping

The present framework was finally applied to map the process–structure–property (PSP) space of the (P,v) domain. We considered a zig-zag scanning strategy with a ±90° rotation between successive layers and a hatching distance of 100 µm. Laser power (P) was varied from 100 to 500 W and scanning speed (v) from 200 to 900 mm·s^{-1}, with regular intervals of 50 W and 50 mm·s^{-1}, respectively. For each condition, single-track thermal simulations were performed, followed by CA and CPFE simulations, using the same procedures and model sizes as described previously.

Based on the single-track thermal simulation results, the (P, v) process space was initially segmented into four distinct regions: keyhole, lack of fusion, balling, and good printing. Keyhole mode was defined as occurring when the depth-to-width ratio (d/w) exceeded 1.5 [60]. Lack of fusion was determined based on a geometric criterion involving the layer thickness (t), hatching distance (h), and melt pool width (w) and depth (d) [61]:

$$w\sqrt{1-\frac{t}{t+d}} < h. \tag{19}$$

The onset of balling can, in principle, be predicted from thermal-field data by introducing a capillary instability criterion. Specifically, according to the classical Plateau–Rayleigh relation, when the ratio of melt-pool length (L) to its depth (d) exceeds π,

$$\frac{L}{d} \geq \pi \tag{20}$$

the molten track becomes unstable [2]. This provides a first-order estimate for the transition between stable and unstable melt-pool morphologies. The required L and d values can be extracted directly from our thermal simulations, enabling the identification of potentially unstable conditions without additional experiments. However, as also noted in recent studies [62], the strict $L/d \geq \pi$ threshold tends to produce a conservative "good printing" region. Adjusting this threshold based on experimental data may yield more accurate predictions. Thus, balling was defined empirically from single-track experiments, where it was observed for $P > 300$ W and $v > 900$ mm·s^{-1} [47]. Any condition not falling into these three categories was classified as a "good printing" condition.

Fig. 15(a–c) shows the domain decomposition using a Support Vector Machine (SVM) algorithm for classification. Data from previous thermal simulations were also included to aid this classification. The predicted "good printing" condition agrees well with the experimentally validated process window previously reported in the literature [47]. CA simulations were subsequently performed for all identified "good printing" conditions. Fig. 15(d) reports cross-sectional EBSD maps on the xy-plane with IPF color coding along the z-direction for these conditions. The "good printing" domain in Fig. 15(a) is colored with the M-index values estimated from these maps, using thin-plate spline interpolation. From these results, three distinct microstructural regions can be identified. At low power and velocity conditions ($P \leq 150$ W, $v \leq 250$ mm·s^{-1}), a near-single-crystal microstructure is predicted, with an M-index close to 0.8. For higher power and scan velocities, conditions near the keyhole domain ($P/v > 0.4$ W/(mm·s^{-1})) tend to generate a chessboard-like microstructure with a moderately strong $\{001\}_z\langle100\rangle_x$ texture, where individual squares are nearly single crystals. In the remaining region ($P/v < 0.4$ W/(mm·s^{-1})), the regular chessboard pattern progressively fades as the lack-of-fusion region is approached. Here, the microstructure is predominantly composed of fine grains with random orientations, leading to an M-index near zero. This is attributed to a high cooling rate that inhibits epitaxial growth from both the bottom of the melt pool and subsequent layers.

The Young's modulus and yield stress, predicted from the CPFE simulations of the cubic RVEs extracted from each CA microstructure, are reported in Fig. 15(b and c). The results show that the single-crystal region exhibits the lowest Young's modulus (approximately 100 GPa), while the fine-grain domain with a near-random texture shows the highest Young's modulus (ranging from 210–225 GPa). Similarly, the

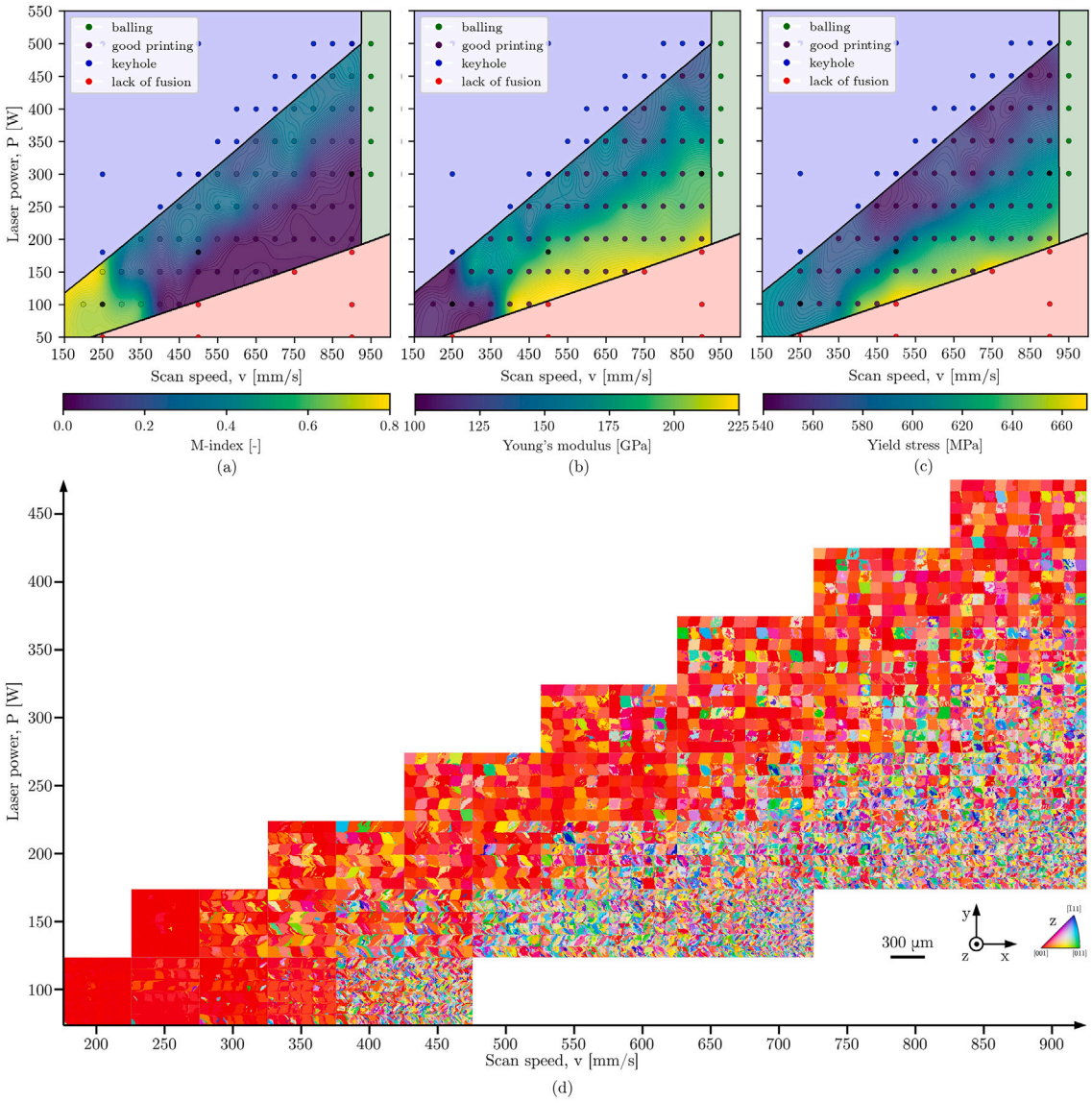

Fig. 15. Process parameter maps considering balling, keyholing and lack of fusion criteria estimated by SVM classifier with (a) the M-index, (b) the Young's modulus and (c) the yield stress distribution in the good printing conditions predicted by CA and CPFE simulations. (d) Cross-section EBSD maps with IPF color coding along the z-direction on the xy-plane of the predicted microstructures.

yield stress is highest in the fine-grain region. Surprisingly, however, it is the lowest in the columnar grain region, not the single-crystal region. It is important to note that the present CP model employs a local formulation and does not account for size effects; the CRSS and hardening parameters are identical for all grains. Therefore, the observed changes in yield stress are solely attributable to the effects of crystallographic texture and grain-to-grain interactions.

The yield strengths predicted by the CPFE simulations are consistent with the ranges of experimental results reported for LPBF-processed Hastelloy X alloys, with fine-grained microstructures exhibiting yield stresses of approximately 620 MPa and coarse-grained ones around 500 MPa [63,64]. The predicted strength levels in the present study therefore fall within or above these experimentally validated ranges, confirming that the simulated microstructures capture the dominant texture- and grain-morphology-driven deformation behavior. It should be noted, however, that the current CP model does not include explicit damage or failure mechanisms and is thus not intended to quantitatively predict the ultimate tensile strength or elongation to failure. An important advantage of the proposed ICME framework lies in its efficiency: once calibrated, the workflow can explore wide combinations of laser parameters and scanning strategies within hours, whereas equivalent experimental campaigns typically require weeks of sample preparation, microstructural characterization, and mechanical testing. This significantly reduces experimental effort while retaining the capability to mechanistically link processing conditions, microstructure, and mechanical response.

4. Conclusions

In the present work, an experimental-numerical integrated framework was proposed for the mapping of the PSP relationship in AM materials, with an application on Hastelloy-X alloy. By coupling heat transfer, CA and CPFE models, a digital twin capable of predicting both microstructure and mechanical properties across a wide range of processing conditions was established. The key findings from this integrated framework are summarized as follows:

1. The thermal model, calibrated via single-track experiments and Bayesian inference, effectively captured the transition from

conduction to keyhole melting. Accurate prediction relied on dynamically adjusting laser absorptivity based on melt pool geometry and a critical volumetric shape parameter (m).
2. The CA simulations accurately reproduced key microstructural features, including the transition from fine, equiaxed grains to a dominant columnar structure and the formation of a strong $\{001\}_z\langle 100\rangle_x$ texture. These simulations confirmed that the microstructure is predominantly controlled by epitaxial growth rather than nucleation density.
3. CPFE simulations revealed a strong link between crystallographic texture and mechanical properties. The highest Young's modulus and yield stress were found in the fine-grain region, while the lowest yield stress occurred in the columnar region, highlighting the important role of texture and grain interactions.

The most significant outcome of this ICME framework is its ability to systematically predict microstructures and properties across an entire process map, offering a viable and efficient alternative to costly, time-consuming experimental trial-and-error. This capability paves the way for data-driven optimization of AM processes. Future work will extend the framework's capabilities to provide a more comprehensive prediction of component performance. This will involve integrating a defect prediction module to model the formation and impact of critical defects like lack of fusion and porosity on local mechanical properties. Additionally, we will integrate a performance prediction module to assess long-term behavior, such as fatigue and creep.

CRediT authorship contribution statement

Fabien Briffod: Writing – original draft, Methodology, Investigation, Formal analysis, Conceptualization. **Phuangphaga Daram:** Writing – review & editing, Investigation, Data curation. **Masahiro Kusano:** Writing – review & editing, Validation, Investigation, Conceptualization. **Makoto Watanabe:** Writing – review & editing, Validation, Supervision, Resources, Project administration, Conceptualization.

Declaration of competing interest

The authors declare that they have no known competing financial interests or personal relationships that could have appeared to influence the work reported in this paper.

Acknowledgements

The authors acknowledge Masakazu Tsujii for his assistance with the experiments. This work was partly supported by "Innovative Science and Technology Initiative for Security, Grant Number JPJ004596 implemented by the Acquisition, Technology, and Logistics Agency (ATLA), Japan". This work was partially supported by JSPS KAKENHI Grant Number 24K07230.

Appendix A. Supplementary data

Supplementary data for this article can be found online at doi:10.1016/j.matdes.2025.115097.

Data availability

Data will be made available upon request.

References

[1] W.E. Frazier, Metal additive manufacturing: a review, J. Mater. Eng. Perform. 23 (2014) 1917–1928, https://doi.org/10.1007/s11665-014-0958-z
[2] T. DebRoy, H.L. Wei, J.S. Zuback, T. Mukherjee, J.W. Elmer, J.O. Milewski, A.M. Beese, A. Wilson-Heid, A. De, W. Zhang, Additive manufacturing of metallic components – process, structure and properties, Prog. Mater. Sci. 92 (2018) 112–224, https://doi.org/10.1016/j.pmatsci.2017.10.001
[3] G. Liu, X. Zhang, X. Chen, Y. He, L. Cheng, M. Huo, J. Yin, F. Hao, S. Chen, P. Wang, S. Yi, L. Wan, Z. Mao, Z. Chen, X. Wang, Z. Cao, J. Lu, Additive manufacturing of structural materials (July 2021) https://doi.org/10.1016/j.mser.2020.100596
[4] A. Vafadar, F. Guzzomi, A. Rassau, K. Hayward, Advances in metal additive manufacturing: a review of common processes, industrial applications, and current challenges (Feb. 2021) https://doi.org/10.3390/app11031213
[5] B. Blakey-Milner, P. Gradl, G. Snedden, M. Brooks, J. Pitot, E. Lopez, M. Leary, F. Berto, A. du Plessis, Metal additive manufacturing in aerospace: a review, Mater. Des. 209 (Nov. 2021) https://doi.org/10.1016/j.matdes.2021.110008
[6] G.L. Knapp, T. Mukherjee, J.S. Zuback, H.L. Wei, T.A. Palmer, A. De, T. DebRoy, Building blocks for a digital twin of additive manufacturing, Acta Mater. 135 (2017) 390–399, https://doi.org/10.1016/j.actamat.2017.06.039
[7] W. Yan, Y. Lian, C. Yu, O.L. Kafka, Z. Liu, W.K. Liu, G.J. Wagner, An integrated process–structure–property modeling framework for additive manufacturing, Comput. Methods Appl. Mech. Eng. 339 (2018) 184–204, https://doi.org/10.1016/j.cma.2018.05.004
[8] C. Herriott, X. Li, N. Kouraytem, V. Tari, W. Tan, B. Anglin, A.D. Rollett, A.D. Spear, A multi-scale, multi-physics modeling framework to predict spatial variation of properties in additive-manufactured metals, Modell. Simul. Mater. Sci. Eng. 27 (Jan. 2019) https://doi.org/10.1088/1361-651X/aaf753
[9] N. Kouraytem, X. Li, W. Tan, B. Kappes, A.D. Spear, Modeling process-structure-property relationships in metal additive manufacturing: a review on physics-driven versus data-driven approaches (July 2021) https://doi.org/10.1088/2515-7639/abca7b
[10] M. Bayat, W. Dong, J. Thorborg, A.C. To, J.H. Hattel, A review of multi-scale and multi-physics simulations of metal additive manufacturing processes with focus on modeling strategies (Nov. 2021) https://doi.org/10.1016/j.addma.2021.102278
[11] V. Romanova, M.S. Mohebbi, E. Dymnich, R. Balokhonov, V. Ploshikhin, A physically-based computational approach for processing-microstructure-property linkage of materials additively manufactured by laser powder bed fusion, Int. J. Mech. Sci. 219 (Apr. 2022) https://doi.org/10.1016/j.ijmecsci.2022.107103
[12] O. Zinovieva, V. Romanova, E. Dymnich, A. Zinoviev, R. Balokhonov, A review of computational approaches to the microstructure-informed mechanical modelling of metals produced by powder bed fusion additive manufacturing (Oct. 2023) https://doi.org/10.3390/ma16196459
[13] T. Shen, B. Li, J. Zhang, F. Xuan, Integrated computational materials engineering (ICME) for predicting tensile properties of additively manufactured defect-free single-phase high-entropy alloy, Virt. Phys. Prototyp. 20 (2025) https://doi.org/10.1080/17452759.2024.2441947
[14] P.S. Cook, A.B. Murphy, Simulation of melt pool behaviour during additive manufacturing: underlying physics and progress (Jan. 2020) https://doi.org/10.1016/j.addma.2019.100909
[15] P. Promoppatum, S.C. Yao, P.C. Pistorius, A.D. Rollett, A comprehensive comparison of the analytical and numerical prediction of the thermal history and solidification microstructure of Inconel 718 products made by laser powder-bed fusion, Engineering 3 (2017) 685–694, https://doi.org/10.1016/J.ENG.2017.05.023
[16] W. Keeley, R. Turner, B. Mitchell, N. Warnken, A development of the Rosenthal equation for predicting thermal profiles during additive manufacturing, Thermo 5 (2025) 16, https://doi.org/10.3390/thermo5020016
[17] M. Kusano, H. Kitano, M. Watanabe, Novel calibration strategy for validation of finite element thermal analysis of selective laser melting process using Bayesian optimization, Materials 14 (Sept. 2021) https://doi.org/10.3390/ma14174948
[18] M. Kusano, M. Watanabe, Heat source model development for thermal analysis of laser powder bed fusion using Bayesian optimization and machine learning, Integr. Mater. Manuf. Innov. 13 (2024) 288–304, https://doi.org/10.1007/s40192-023-00334-2
[19] A. Zinoviev, O. Zinovieva, V. Ploshikhin, V. Romanova, R. Balokhonov, Evolution of grain structure during laser additive manufacturing. Simulation by a cellular automata method, Mater. Des. 106 (2016) 321–329, https://doi.org/10.1016/j.matdes.2016.05.125
[20] O. Zinovieva, A. Zinoviev, V. Ploshikhin, Three-dimensional modeling of the microstructure evolution during metal additive manufacturing, Comput. Mater. Sci. 141 (2018) 207–220, https://doi.org/10.1016/j.commatsci.2017.09.018
[21] J. Coleman, G.L. Knapp, B. Stump, M. Rolchigo, K. Kincaid, A. Plotkowski, A dynamic volumetric heat source model for laser additive manufacturing, Addit. Manuf. 95 (Sept. 2024) https://doi.org/10.1016/j.addma.2024.104531
[22] J. Robichaud, T. Vincent, B. Schultheis, A. Chaudhary, Integrated computational materials engineering to predict melt-pool dimensions and 3d grain structures for selective laser melting of Inconel 625, Integr. Mater. Manuf. Innov. 8 (2019) 305–317, https://doi.org/10.1007/s40192-019-00145-4
[23] J. Katagiri, S. Nomoto, M. Kusano, M. Watanabe, Effect of mushy zone constant in Voller-Prakash model on keyholing behaviour in laser powder bed fusion simulation, Results in Engineering 24 (Dec. 2024) https://doi.org/10.1016/j.rineng.2024.103567
[24] W. Kurz, B. Giovanola, R. Trivedi, Theory of microstructural development during rapid solidification, Acta metall. 34 (1986) 823.
[25] A.F. Chadwick, P.W. Voorhees, The development of grain structure during additive manufacturing, Acta Mater. 211 (June 2021) https://doi.org/10.1016/j.actamat.2021.116862
[26] M. Yang, L. Wang, W. Yan, Phase-field modeling of grain evolutions in additive manufacturing from nucleation, growth, to coarsening, npj Comput. Mater. 7 (December 2021) https://doi.org/10.1038/s41524-021-00524-6
[27] T. Xue, Z. Gan, S. Liao, J. Cao, Physics-embedded graph network for accelerating phase-field simulation of microstructure evolution in additive manufacturing, npj Comput. Mater. 8 (Dec. 2022) https://doi.org/10.1038/s41524-022-00890-9
[28] M. Okugawa, K. Saito, H. Yoshima, K. Sawaizumi, S. Nomoto, M. Watanabe, T. Nakano, Y. Koizumi, Solute segregation in a rapidly solidified hastelloy-x ni-based superalloy during laser powder bed fusion investigated by phase-field and

computational thermal-fluid dynamics simulations, Addit. Manuf. 84 (March 2024) https://doi.org/10.1016/j.addma.2024.104079
[29] S. Nomoto, M. Kusano, T. Kitashima, M. Watanabe, Numerical simulation method for the laser powder bed fusion process by lattice boltzmann and multi-phase field methods, Comput. Mater. Sci. 250 (Feb. 2025) https://doi.org/10.1016/j.commatsci.2025.113688
[30] C.-A. Gandin, M. Rappaz, A 3d cellular automaton algorithm for the prediction of dendritic grain growth, Acta Mater. 45 (1997) 2187–2195.
[31] J. Zhang, F. Liou, W. Seufzer, K. Taminger, A coupled finite element cellular automaton model to predict thermal history and grain morphology of Ti-6Al-4V during direct metal deposition (DMD), Addit. Manuf. 11 (2016) 32–39, https://doi.org/10.1016/j.addma.2016.04.004
[32] Y. Lian, Z. Gan, C. Yu, D. Kats, W.K. Liu, G.J. Wagner, A cellular automaton finite volume method for microstructure evolution during additive manufacturing, Mater. Des. 169 (May 2019) https://doi.org/10.1016/j.matdes.2019.107672
[33] O. Zinovieva, A. Zinoviev, V. Romanova, R. Balokhonov, Three-dimensional analysis of grain structure and texture of additively manufactured 316l austenitic stainless steel, Addit. Manuf. 36 (Dec. 2020) https://doi.org/10.1016/j.addma.2020.101521
[34] K. Teferra, D.J. Rowenhorst, Optimizing the cellular automata finite element model for additive manufacturing to simulate large microstructures, Acta Mater. 213 (July 2021) https://doi.org/10.1016/j.actamat.2021.116930
[35] M. Rolchigo, S.T. Reeve, B. Stump, G.L. Knapp, J. Coleman, A. Plotkowski, J. Belak, Exaca: a performance portable exascale cellular automata application for alloy solidification modeling, Comput. Mater. Sci. 214 (Nov. 2022) https://doi.org/10.1016/j.commatsci.2022.111692
[36] X. Liang, J. Zhu, V. Popovich, M. Hermans, I. Richardson, C. Bos, A multi-level capture algorithm for accelerating cellular automata predictions of grain structure and texture in additive manufacturing, Addit. Manuf. 98 (Jan. 2025) https://doi.org/10.1016/j.addma.2024.104622
[37] A. Pineau, G. Guillemot, D. Tourret, A. Karma, C.A. Gandin, Growth competition between columnar dendritic grains – cellular automaton versus phase field modeling, Acta Mater. 155 (2018) 286–301, https://doi.org/10.1016/j.actamat.2018.05.032
[38] E. Dorari, K. Ji, G. Guillemot, C.A. Gandin, A. Karma, Growth competition between columnar dendritic grains – the role of microstructural length scales, Acta Mater. 223 (Jan. 2022) https://doi.org/10.1016/j.actamat.2021.117395
[39] F. Roters, P. Eisenlohr, L. Hantcherli, D.D. Tjahjanto, T.R. Bieler, D. Raabe, Overview of constitutive laws, kinematics, homogenization and multiscale methods in crystal plasticity finite-element modeling: theory, experiments, applications, Acta Mater. 58 (2010) 1152–1211, https://doi.org/10.1016/j.actamat.2009.10.058
[40] B. Liu, D. Raabe, F. Roters, P. Eisenlohr, R.A. Lebensohn, Comparison of finite element and fast Fourier transform crystal plasticity solvers for texture prediction, Modell. Simul. Mater. Sci. Eng. 18 (Dec. 2010) https://doi.org/10.1088/0965-0393/18/8/085005
[41] M. Yaghoobi, S. Ganesan, S. Sundar, A. Lakshmanan, S. Rudraraju, J.E. Allison, V. Sundararaghavan, Prisms-plasticity: an open-source crystal plasticity finite element software, Comput. Mater. Sci. 169 (Nov. 2019) https://doi.org/10.1016/j.commatsci.2019.109078
[42] F. Roters, M. Diehl, P. Shanthraj, P. Eisenlohr, C. Reuber, S.L. Wong, T. Maiti, A. Ebrahimi, T. Hochrainer, H.O. Fabritius, S. Nikolov, M. Friák, N. Fujita, N. Grilli, K.G.F. Janssens, N. Jia, P.J.J. Kok, D. Ma, F. Meier, E. Werner, M. Stricker, D. Weygand, D. Raabe, Damask – the düsseldorf advanced material simulation kit for modeling multi-physics crystal plasticity, thermal, and damage phenomena from the single crystal up to the component scale, Comput. Mater. Sci. 158 (2019) 420–478, https://doi.org/10.1016/j.commatsci.2018.04.030
[43] M. Rolchigo, R. Carson, J. Belak, Understanding uncertainty in microstructure evolution and constitutive properties in additive process modeling, Metals 12 (2) (2022) https://doi.org/10.3390/met12020324
[44] J. Ye, S.A. Khairallah, A.M. Rubenchik, M.F. Crumb, G. Guss, J. Belak, M.J. Matthews, Energy coupling mechanisms and scaling behavior associated with laser powder bed fusion additive manufacturing, Adv. Eng. Mater. 21 (7) (2019) https://doi.org/10.1002/adem.201900185
[45] Z. Gan, O.L. Kafka, N. Parab, C. Zhao, L. Fang, O. Heinonen, T. Sun, W.K. Liu, Universal scaling laws of keyhole stability and porosity in 3d printing of metals, Nat. Commun. 12 (Dec. 2021) https://doi.org/10.1038/s41467-021-22704-0
[46] J.S. Weaver, J.C. Heigel, B.M. Lane, Laser spot size and scaling laws for laser beam additive manufacturing, J. Manuf. Process. 73 (2022) 26–39, https://doi.org/10.1016/j.jmapro.2021.10.053
[47] H. Kitano, M. Kusano, M. Tsujii, A. Yumoto, M. Watanabe, Process parameter optimization framework for the selective laser melting of Hastelloy X alloy considering defects and solidification crack occurrence, Crystals 11 (6) (2021) https://doi.org/10.3390/cryst11060578
[48] K.C. Mills, Recommended Values of Thermophysical Properties for Selected Commercial Alloys, Woodhead, 2002.
[49] D.S. Bulgarevich, M. Watanabe, Stress–strain curve predictions by crystal plasticity simulations and machine learning, Sci. Rep. 14 (Dec. 2024) https://doi.org/10.1038/s41598-024-80098-7
[50] P. Daram, M. Kusano, M. Watanabe, Investigation of the process optimization for L-PBF Hastelloy X alloy on microstructure and mechanical properties, Materials 18 (April 2025) https://doi.org/10.3390/ma18081890
[51] M. Rolchigo, B. Stump, J. Belak, A. Plotkowski, Sparse thermal data for cellular automata modeling of grain structure in additive manufacturing, Modell. Simul. Mater. Sci. Eng. 28 (Sept. 2020) https://doi.org/10.1088/1361-651X/ab9734
[52] E.H. Lee, D.T. Liu, Finite-strain elastic - plastic theory with application to plane-wave analysis, J. Appl. Phys. 38 (1967) 19–27, https://doi.org/10.1063/1.1708953
[53] C.M. Pilgar, A.M. Fernandez, S. Lucarini, J. Segurado, Effect of printing direction and thickness on the mechanical behavior of SLM fabricated hastelloy-x, Int. J. Plast. 153 (June 2022) https://doi.org/10.1016/j.ijplas.2022.103250
[54] T. Ishimoto, K. Hagihara, K. Hisamoto, T. Nakano, Stability of crystallographic texture in laser powder bed fusion: understanding the competition of crystal growth using a single crystalline seed, Addit. Manuf. 43 (July 2021) https://doi.org/10.1016/j.addma.2021.102004
[55] T. Ishimoto, N. Morita, R. Ozasa, A. Matsugaki, O. Gokcekaya, S. Higashino, M. Tane, T. Mayama, K. Cho, H.Y. Yasuda, M. Okugawa, Y. Koizumi, M. Yoshiya, D. Egusa, T. Sasaki, E. Abe, H. Kimizuka, N. Ikeo, T. Nakano, Superimpositional design of crystallographic textures and macroscopic shapes VIA metal additive manufacturing—game-change in component design, Acta Mater. 286 (Mar. 2025) https://doi.org/10.1016/j.actamat.2025.120709
[56] D.E. Jodi, T. Kitashima, Y. Koizumi, T. Nakano, M. Watanabe, Manufacturing single crystals of pure nickel VIA selective laser melting with a flat-top laser beam, Addit. Manuf. Lett. 3 (Dec. 2022) https://doi.org/10.1016/j.addlet.2022.100066
[57] P. Skemer, I. Katayama, Z. Jiang, S.I. Karato, The misorientation index: development of a new method for calculating the strength of lattice-preferred orientation, Tectonophysics 411 (2005) 157–167, https://doi.org/10.1016/j.tecto.2005.08.023
[58] Z. Dong, P. Ouyang, S. Zhang, L. Liu, H. Li, Y. Wu, Effect of building direction on anisotropy of mechanical properties of GH4169 alloy fabricated by laser powder bed fusion, Mater. Sci. Eng. A 862 (Jan. 2023) https://doi.org/10.1016/j.msea.2022.144430
[59] R. Lai, J. Zhao, L. Lei, L. Shi, S. Wu, X. Zhang, Revealing the tensile anisotropic mechanisms of additive manufactured IN718 alloy based on crystal plasticity modeling, Comput. Mater. Sci. 251 (2025) 113735, https://doi.org/10.1016/j.commatsci.2025.113735
[60] J.D. Roehling, A. Perron, J.L. Fattebert, T. Haxhimali, G. Guss, T.T. Li, D. Bober, A.W. Stokes, A.J. Clarke, P.E.A. Turchi, M.J. Matthews, J.T. McKeown, Rapid solidification in bulk Ti-Nb alloys by single-track laser melting, JOM 70 (2018) 1589–1597, https://doi.org/10.1007/s11837-018-2920-2
[61] R. Seede, D. Shoukr, B. Zhang, A. Whitt, S. Gibbons, P. Flater, A. Elwany, R. Arroyave, I. Karaman, An ultra-high strength martensitic steel fabricated using selective laser melting additive manufacturing: densification, microstructure, and mechanical properties, Acta Mater. 186 (2020) 199–214, https://doi.org/10.1016/j.actamat.2019.12.037
[62] J. Katagiri, M. Kusano, S. Minamoto, H. Kitano, K. Daimaru, M. Tsujii, M. Watanabe, Melt pool shape evaluation by single-track experiments and finite-element thermal analysis: balling and lack of fusion criteria for generating process window of inconel738lc, Materials 16 (Feb. 2023) https://doi.org/10.3390/ma16041729
[63] M.L. Montero-Sistiaga, S. Pourbabak, J. Van Humbeeck, D. Schryvers, K. Vanmeensel, Microstructure and mechanical properties of Hastelloy X produced by HP-SLM (high power selective laser melting), Mater. Des. 165 (Mar. 2019) https://doi.org/10.1016/j.matdes.2019.107598
[64] M.L. Montero-Sistiaga, Z. Liu, L. Bautmans, S. Nardone, G. Ji, J.P. Kruth, J. Van Humbeeck, K. Vanmeensel, Effect of temperature on the microstructure and tensile properties of micro-crack free Hastelloy X produced by selective laser melting, Addit. Manuf. 31 (Jan. 2020) https://doi.org/10.1016/j.addma.2019.100995